IOP Publishing Journal of Optics
J. Opt. 19 (2017) 085504 (9pp) https://doi.org/10.1088/2040-8986/aa792d

Label-free super-resolution with coherent nonlinear structured-illumination microscopy

Mikko J Huttunen[1], Aazad Abbas[1], Jeremy Upham[1] and Robert W Boyd[1,2]

[1] Department of Physics, University of Ottawa, Ottawa, Ontario K1N 6N5, Canada
[2] The Institute of Optics and Department of Physics and Astronomy, University of Rochester, Rochester, NY14627, United States of America

E-mail: mikkojhuttunen@gmail.com

Received 1 March 2017, revised 25 April 2017
Accepted for publication 13 June 2017
Published 18 July 2017

Abstract

Structured-illumination microscopy enables up to a two-fold lateral resolution improvement by spatially modulating the intensity profile of the illumination beam. We propose a novel way to generalize the concept of structured illumination to nonlinear widefield modalities by spatially modulating, instead of field intensities, the phase of the incident field while interferometrically measuring the complex-valued scattered field. We numerically demonstrate that for second-order and third-order processes an almost four- and six-fold increase in lateral resolution is achievable, respectively. This procedure overcomes the conventional Abbe diffraction limit and provides new possibilities for label-free super-resolution microscopy.

Keywords: super-resolution, microscopy, optical transfer functions, harmonic generation, second-harmonic generation, third-harmonic generation

(Some figures may appear in colour only in the online journal)

1. Introduction

All conventional optical microscopy modalities are restricted by the Abbe diffraction limit [1], which dictates the achievable spatial resolution. Within far-field microscopy, a range of super-resolution techniques based on fluorescent molecules has been developed to overcome the diffraction limit [2]. Such techniques include stimulated emission depletion microscopy [3, 4], photoactivated localization microscopy [5], stochastic optical resolution microscopy [6] and the many variants of conventional confocal microscopy [7, 8]. Of particular interest to this work is structured-illumination microscopy (SIM) [9, 10]. In SIM the spatial intensity modulation of the illumination beam is used to extend the range of collected spatial frequencies from the object and to consequently improve the spatial resolution of the formed image. Regular linear SIM can double the achievable lateral resolution, while the saturable behavior of fluorophores can almost quadruple the resolution [11–13].

Despite being based on different working principles, all of these super-resolution techniques require the use of staining and fluorescent labels. But since the use of labels can complicate and limit the possibilities in some applications [14–17], label-free super-resolution techniques could be beneficial. A few optical label-free techniques have been recently proposed [19–21], but they produce only up to two-fold resolution increase. The need persists for new techniques that provide better resolution, good contrast and impose fewer restrictions on the object.

In nonlinear optical processes several fields interact with matter, typically creating new frequency components [22, 23]. In the process of second-harmonic generation (SHG), two fields at the fundamental frequency ω are converted into a new field with a doubled frequency 2ω. Similarly, in the process of third-harmonic generation (THG), three incident fields at the fundamental frequency ω are converted to a new field with a tripled frequency 3ω. These and other nonlinear processes make use of the intrinsic nonlinear response of the object under investigation and can thus be used for label-free

imaging [24–31]. Since the release of these pioneering works, SHG and THG microscopy modalities have evolved into useful tools to study biological samples in label-free manner. In particular, SHG microscopy can provide useful information of tissue morphology for diagnostic applications [14, 15], while THG microscopy can be used, for example, to study organization of lipid molecules [16–18]. A few nonlinear super-resolution techniques have been proposed, but the demonstrated lateral resolution has been no better than of the order of three times the diffraction limit [32–38].

In this paper, we propose and numerically analyze a new scheme for achieving super-resolution based on the intrinsic coherent nonlinear processes, such as SHG or THG, occurring in the object. The approach is based on the SIM scheme where, instead of light intensities, the phase of the incident field is modulated and the complex-valued emitted field is interferometrically measured. We lay out the mathematical framework and perform simulations to show that an almost four-fold (six-fold) resolution increase is achievable for second-order (third-order) processes. Also when compared to conventional laser-scanning SHG or THG microscopies, the achievable lateral resolution is shown to be considerably improved. Our results therefore open new possibilities for label-free imaging.

2. Theory

In regular incoherent SIM, the intensity modulation of the illumination beam can be used to extend the range of spatial frequencies collected from the object [9, 10]. This is based on the fact that an incoherent imaging system is approximately a linear translation-invariant system in terms of the emitted and detected intensity distributions. Our scheme is based on coherent nonlinear processes. The relevant imaging system is then approximately a linear translation-invariant system in terms of the emitted and detected fields. The advantage of nonlinear coherent SIM is that by phase-modulating the incident field and imaging the complex-valued emitted field, even higher spatial frequencies can be collected by utilizing nonlinear optical processes. Therefore, the lateral resolution can be improved by a larger factor compared to previous coherent SIM schemes [19–21]. For SHG-SIM the lateral resolution can be increased almost four-fold, whereas an almost six-fold increase is possible for THG-SIM. We believe, that similar increase of resolution could be achievable also for the process of coherent anti-Stokes Raman scattering (CARS) [39, 40].

In a coherent widefield imaging system, the incident field $E_{\mathrm{inc}}(\omega, \mathbf{r})$ oscillating at a carrier frequency ω illuminates the object, interacts with it and is emitted given by

$$E_{\mathrm{em}}(\omega, \mathbf{r}) = s(\omega, \mathbf{r})E_{\mathrm{inc}}(\omega, \mathbf{r}), \tag{1}$$

where $E_{\mathrm{em}}(\omega, \mathbf{r})$ is the emitted field and $s(\omega, \mathbf{r})$ is the response function of the object. By imaging the emitted field $E_{\mathrm{em}}(\omega, \mathbf{r})$ spatial information of the object response $s(\omega, \mathbf{r})$ can then be acquired. Assuming that the imaging system in question is free from aberrations, is linear and is translation-invariant, the image formation process can be described as a linear translation-invariant system. The detected image field $E_{\mathrm{det}}(\omega, \mathbf{r})$ is then a convolution of the emitted field $E_{\mathrm{em}}(\omega, \mathbf{r})$ and the coherent point-spread function $\mathrm{PSF}(\omega, \mathbf{r})$ of the system given as

$$E_{\mathrm{det}}(\omega, \mathbf{r}) = \int\int_{-\infty}^{\infty} E_{\mathrm{em}}(\omega, \mathbf{r}')\mathrm{PSF}(\omega, \mathbf{r} - \mathbf{r}')\mathrm{d}\mathbf{r}'. \tag{2}$$

We next switch to the spatial-frequency domain by defining the Fourier transform (FT) and the inverse FT as

$$\mathbf{E}(\mathbf{k}) = \int\int_{-\infty}^{\infty} \mathbf{E}(\mathbf{r})\mathrm{e}^{-\mathrm{i}\mathbf{k}\cdot\mathbf{r}}\mathrm{d}\mathbf{r}, \tag{3}$$

$$\mathbf{E}(\mathbf{r}) = \frac{1}{4\pi^2}\int\int_{-\infty}^{\infty} \mathbf{E}(\mathbf{k})\mathrm{e}^{\mathrm{i}\mathbf{k}\cdot\mathbf{r}}\mathrm{d}\mathbf{k}, \tag{4}$$

where $\mathbf{E}(\mathbf{r})$ is the optical field and $\mathbf{E}(\mathbf{k})$ is the FT of the field. In the spatial-frequency domain the detected image field $E_{\mathrm{det}}(\omega, \mathbf{k})$ becomes a point-wise multiplication of the respective FTs

$$E_{\mathrm{det}}(\omega, \mathbf{k}) = E_{\mathrm{em}}(\omega, \mathbf{k})\mathrm{CTF}(\omega, \mathbf{k}), \tag{5}$$

where $E_{\mathrm{em}}(\omega, \mathbf{k})$ is the FT of the emitted field and the coherent transfer function $\mathrm{CTF}(\omega, \mathbf{k})$ is the FT of the PSF. It is the CTF that dictates the achievable resolution by limiting the highest detectable transverse spatial-frequency component k_{max} passing the system [1, 9]. The minimum resolvable feature size d using the system is determined by

$$d = \frac{\lambda}{2\mathrm{NA}} = \frac{1}{2k_{\mathrm{max}}}, \tag{6}$$

where λ is the wavelength of the light traveling through the objective in vacuum and NA is the numerical aperture of the imaging lens.

Next we consider what happens if $E_{\mathrm{inc}}(\omega, \mathbf{r})$ is not spatially uniform but instead has some modulation applied to the phase of the field given as

$$E_{\mathrm{inc}}(\omega, \mathbf{r}) = E_0(\omega, \mathbf{r})\exp(-\mathrm{i}\mathbf{k}' \cdot \mathbf{r}), \tag{7}$$

where $E_0(\omega, \mathbf{r})$ is a spatially uniform illumination pattern and $\mathbf{k}'$ is the modulation wave vector. The modulation will consequently affect E_{em}. Specifically, a shift by $\mathbf{k}'$ is seen in the spatial-frequency representation of the emitted field given by

$$E_{\mathrm{em}}(\omega, \mathbf{k}) = E'_{\mathrm{em}}(\mathbf{k} + \mathbf{k}'), \tag{8}$$

where E'_{em} is the emitted field due to the illumination $E_0(\omega, \mathbf{r})$. Looking at (5) and (8), we see that higher spatial frequencies in the direction along $\mathbf{k}'$ can be detected. By setting $\|\mathbf{k}'\| = k_{\mathrm{max}}$ and modulating in multiple directions, all the higher components $< \|2k_{\mathrm{max}}\|$ can be collected to effectively double the extent of the CTF and thus the lateral resolution. The resulting resolution improvement is similar to that of incoherent SIM. Next we show how the nonlinear optical response of the object can improve things further.

For the same modulated incident field E_{inc} as in (7), the SHG and THG response of the object can be described by nonlinear source polarization terms as [22]

$$P_i(2\omega, \mathbf{r}) = \sum_{ijk} \chi^{(2)}_{ijk}(2\omega, \mathbf{r})E_{\mathrm{inc},j}(\mathbf{r})E_{\mathrm{inc},k}(\mathbf{r}), \tag{9}$$

$$P_i(3\omega, \mathbf{r}) = \sum_{ijkl} \chi^{(3)}_{ijkl}(3\omega, \mathbf{r}) \times E_{\mathrm{inc},j}(\mathbf{r}) E_{\mathrm{inc},k}(\mathbf{r}) E_{\mathrm{inc},l}(\mathbf{r}), \quad (10)$$

where $\chi^{(2)}_{ijk}(2\omega, \mathbf{r})$ and $\chi^{(3)}_{ijkl}(3\omega, \mathbf{r})$ are the second- and third-order nonlinear susceptibility tensors, respectively, and $E_{\mathrm{inc},j}(\mathbf{r})$ is the jth component of the incident field at the fundamental frequency ω. For simplicity, we next assume that the incident field is linearly polarized and that the nonlinear material responses are dominated by the tensor components related to the direction along the oscillating field (i.e. for an incident field polarized along the $\hat{i}$ the components $\chi^{(2)}_{iii}$ and $\chi^{(3)}_{iiii}$ dominate). The incident field and the susceptibilities then become scalars and by noting that $E_{\mathrm{em}}(\omega') = \chi(\omega')^{-1} P(\omega')$, where $\omega' = 2\omega$ ($\omega' = 3\omega$) for SHG (THG), we can write the emitted field components at frequencies 2ω and 3ω as

$$E_{\mathrm{em}}(2\omega, \mathbf{r}) = \chi^{-1}(2\omega, \mathbf{r}) \chi^{(2)} \times (2\omega, \mathbf{r}) E_{\mathrm{inc}}(\mathbf{r}) E_{\mathrm{inc}}(\mathbf{r}), \quad (11)$$

$$E_{\mathrm{em}}(3\omega, \mathbf{r}) = \chi^{-1}(3\omega, \mathbf{r}) \chi^{(3)} \times (3\omega, \mathbf{r}) E_{\mathrm{inc}}(\mathbf{r}) E_{\mathrm{inc}}(\mathbf{r}) E_{\mathrm{inc}}(\mathbf{r}), \quad (12)$$

where $\chi^{-1}(2\omega)$ and $\chi^{-1}(3\omega)$ are the inverses of the linear susceptibilities at the given frequencies. If we once again consider these field components in the spatial-frequency domain given by

$$E_{\mathrm{em}}(2\omega, \mathbf{k}) = E'_{\mathrm{em}}(2\omega, \mathbf{k} + \mathbf{2k}'), \quad (13)$$

$$E_{\mathrm{em}}(3\omega, \mathbf{k}) = E'_{\mathrm{em}}(3\omega, \mathbf{k} + \mathbf{3k}'), \quad (14)$$

where the E'_{em} is the emitted field due to $E_0(\omega, \mathbf{r})$, we see that the the total effective CTF can be extended even further by phase modulation. Note that the collected SHG and THG signals have shorter wavelengths and thus, according to (6), proportionally larger k_{max}. The final step is to develop means to measure E_{det}, which can be achieved for example interferometrically [41]. The detected field $E_{\mathrm{det}}(\mathbf{r})$ at the back aperture of the collection objective corresponds to the FT of the image field $E_{\mathrm{det}}(\mathbf{k})$. Therefore, if this field is imaged into a plane of interest where it interferes with a reference field $E_{\mathrm{ref}}(\mathbf{r}) = \|E_{\mathrm{ref}}(\mathbf{r})\| \exp(-\mathrm{i}\phi_{\mathrm{ref}})$ with a known transverse field profile, an intensity pattern I_{det} is created as

$$I_{\mathrm{det}}(\mathbf{r}) = \|E_{\mathrm{det}} + E_{\mathrm{ref}}\|^2 = \|E_{\mathrm{det}}\|^2 + \|E_{\mathrm{ref}}\|^2 + 2\|E_{\mathrm{det}}\|\|E_{\mathrm{ref}}\| \cos(\Delta\phi). \quad (15)$$

Then by changing the relative phase $\Delta\phi = \phi_{\mathrm{det}} - \phi_{\mathrm{ref}}$ between the reference and the detected fields and measuring the respective interference patterns the complex-valued $E_{\mathrm{det}}(\mathbf{k})$ can be reconstructed. We use four relative reference phases ϕ_{ref} and the respective interference patterns to reconstruct $E_{\mathrm{det}}(\mathbf{k})$. After reconstruction, the field can be used to effectively extend the total CTF as explained next.

For simplicity, we assume that the CTF of the imaging system is a uniform disk with the radius limited by the highest detectable transverse spatial frequency component k_{max}, as is illustrated in figure 1(a). Note that for actual experimental work, characterization of the CTF might be needed to correct for aberrations. For simplicity, the procedure is explained only for SHG-SIM, but the approach is readily generalized to other processes and modalities such as THG-SIM resulting in more extended total CTFs and thus better lateral resolution.

The detected second-harmonic image field $E_{\mathrm{det},0}(2\omega, \mathbf{k})$ due to an unmodulated incident fundamental field $E_{\mathrm{inc},0}(\omega, \mathbf{r}) = E_0(\mathbf{r})$ is first measured as explained above. Then the phase of the incident field is modulated as $E_{\mathrm{inc},1}(\mathbf{r}) = E_0(\mathbf{r}) \exp(-\mathrm{i}\mathbf{k}'_1 \cdot \mathbf{r})$ such that $\|\mathbf{k}'\| = k_{\mathrm{max}}(\omega)$ and the respective detected image field $E_{\mathrm{det},1}(2\omega, \mathbf{k})$ is measured and superimposed in the reciprocal space with the initial detected image field (magenta dotted circle in figure 1(b)). The correct shift is found by calculating the correlation between $E_{\mathrm{det},0}(2\omega, \mathbf{k})$ and the shifted $E_{\mathrm{det},1}(2\omega, \mathbf{k})$ at the intersection of the distributions (marked as darker gray region in figure 1(b)). The correlation between the common pixels is maximized at the correct position of the shifted $E_{\mathrm{det},1}(2\omega, \mathbf{k})$, and the relative complement of $E_{\mathrm{det},1}(2\omega, \mathbf{k})$ in $E_{\mathrm{det},0}(2\omega, \mathbf{k})$ can then be added to $E_{\mathrm{det},1}(2\omega, \mathbf{k})$ to extend the support of the total CTF as shown in figure 1(b).

The procedure is repeated for other modulation of the incident field as $E_{\mathrm{inc},j}(\mathbf{r}) = E_0(\mathbf{r}) \exp(-\mathrm{i}\mathbf{k}'_j \cdot \mathbf{r})$ and consequent detected image field $E_{\mathrm{det},j}(2\omega, \mathbf{k})$. Again, the correct position for the field in the reciprocal space is found by calculating the correlation for the pixels in the intersection of the $E_{\mathrm{det},j-1}(2\omega, \mathbf{k})$ (magenta solid line) and the shifted $E_{\mathrm{det},j}(2\omega, \mathbf{k})$ (magenta dotted circle), shown as darker area in figure 1(c). Once the correct location has been found, the relative complement of $E_{\mathrm{det},j}(2\omega, \mathbf{k})$ in $E_{\mathrm{det},j-1}(2\omega, \mathbf{k})$ can then be added to $E_{\mathrm{det},j}(2\omega, \mathbf{k})$ to further extend the total CTF.

This recursive procedure is continued until no further extension of the $E_{\mathrm{det}}(2\omega, \mathbf{k})$ can be achieved. The maximum spatial frequency of the modulation wave vector is restricted by the CTF of the excitation lens $\|\mathbf{k}'\| < k_{\mathrm{max}}$ at the fundamental frequency. But since the emitted field depends on the higher powers of the incident field (see (11) and (12)), the total CTF can be extended further than with traditional coherent SIM. For SHG-SIM the total CTF can be extended almost by a factor of four, as is shown in figure 1(d). Therefore, the lateral resolution of the system is increased by a similar factor. There are two aspects that extend the total CTF. Firstly, the extent of the physical CTF is doubled because the wavelength of the detected field is halved for SHG as shown in figure 1(a). Secondly, the proposed SIM scheme can be used to further double the extent the physical CTF resulting in four-fold extended total CTF.

The data analysis procedure is similar for higher-order nonlinear processes, such as for THG. The main difference is that since the emitted field is more strongly modulated, it is extended further in reciprocal space. Therefore, the total CTF can be extended further than using SHG-SIM. For THG-SIM the total CTF can be extended almost by a factor of six (see figure 1(d)) with a similar increase in the lateral resolution.

3. Results

We perform numerical simulations of the following experimental set-up (see figure 2) that can be used to measure the interference patterns I_{det} as given by (15), which are then used

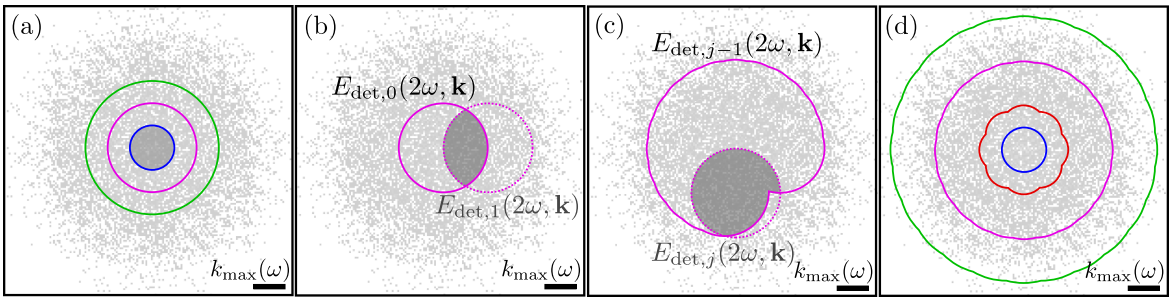

Figure 1. (a) Fourier transform of a sample object. The extent of the physical CTF for fundamental (blue circle), SHG (magenta circle) and THG (green circle) signals are shown. (b) By spatially modulating the incident field, the area of the detected spatial-frequency components is shifted (magenta dotted circle). If the shifted reciprocal image is properly superimposed with the previously detected spatial-frequency components (area inside magenta solid line), a total extended CTF for the system can be formed. The correct location for the shifted reciprocal images can be determined by finding the maximum correlation between the current total CTF (area inside magenta solid line) and the shifted reciprocal image inside the intersection of the distributions (highlighted darker region). (c) The total CTF can be further extended by superimposing shifted reciprocal images of the detected field for different modulations of the incident field. (d) The physical CTF (blue circle) of the system is thus extended by SIM. While linear optical processes can double the extent of the total CTF (red solid line), second (third) -order nonlinear processes can extend the total CTF almost four-fold (six-fold), highlighted with a magenta (green) line.

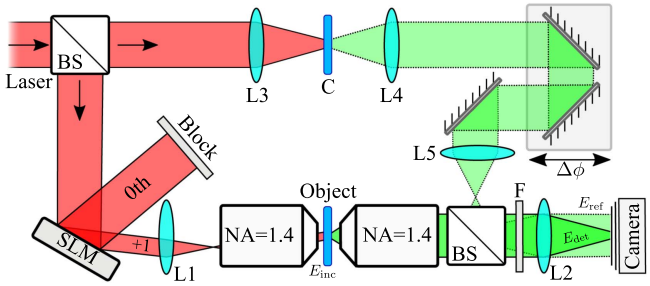

Figure 2. Schematic of the proposed set-up. The incident laser beam is split at the first beam splitter (BS). The object arm beam is spatially phase modulated using a spatial light modulator (SLM) and only the first diffraction order of the modulated beam is imaged by lens L1 onto the back focal plane of the focusing objective to ensure the object is uniformly illuminated. The generated nonlinear emitted field at the back aperture of the collection objective is imaged using lens (L2) to the camera. A reference beam is created in the reference arm using a nonlinear crystal (C) and passed onto the camera. Filter (F) is used to block the fundamental beams. Changing the relative phase ($\Delta\phi$) between the beams and measuring the corresponding interference patterns permits reconstruction of E_{det}.

to reconstruct $E_{\mathrm{det}}(\mathbf{k})$. We assume that incident light with wavelength $\lambda = 1064$ nm and an objective with NA $= 1.4$ are used. The field is phase-modulated using a spatial light modulator and only the first positive diffraction order of the modulated beam is focused to the back focal plane of the focusing objective to ensure that $E_{\mathrm{inc}}(\mathbf{r})$ evenly illuminates and interacts with the object. Then we assume that an identical objective is used to collect the emitted harmonic field components which are imaged using a lens and a camera. To measure $E_{\mathrm{det}}(\mathbf{k})$, we split the original fundamental beam with a beam splitter and pass it through a nonlinear crystal to generate a reference beam $E_{\mathrm{ref}}(\mathbf{r})$. In the case of the coherent SIM no nonlinear crystal is used and the reference beam used for the field reconstruction is the original split beam. To simplify reconstruction of $E_{\mathrm{det}}(\mathbf{k})$, we focus the reference beam into the back focal plane of the imaging lens before the camera, to ensure it is collimated when entering the camera. The delay line (gray area in figure 2) can temporally overlap the two fields and control their relative phase $\Delta\phi$. We reconstruct $E_{\mathrm{det}}(\mathbf{k})$ from the measured interference patterns I_{det} as given by (15), where the phase of the reference field ϕ_{ref} ranges from 0 to almost π. We assume that the interference patterns are measured with a signal-to-noise ratio (SNR) of 300, where the noise was assumed to be normally distributed with the variance proportional to the signal level. This assumption has been found to be a good approximation for relatively weak light levels approaching photon counting regime [42].

The increase in the lateral resolution is seen after the assembled image field $E_{\mathrm{det}}(\mathbf{k})$ is inverse FT into a real image. Simulations of the results are shown in figure 3, where we plot the moduli of the assembled $E_{\mathrm{det}}(\mathbf{k})$ and their inverse FTs. For simplicity, we assume the object is thin, essentially two-dimensional, as shown in figure 3(a), and has feature sizes below 50 nm being clearly smaller than six times the diffraction limit. This is also clear from the modulus of the FT of the object, which contains spatial frequencies with considerably higher magnitude than $k_{\max}$ (see figure 3(b)).

First, we show that the object is poorly resolved using coherent widefield microscopy. Without the use of structured illumination, the features of the image are obviously blurred, due to the Abbe diffraction limit of ~380 nm (see figure 3(c)). Next we simulate how the lateral resolution is increased through use of linear coherent SIM by phase-modulating E_{inc}. We see an almost two-fold resolution improvement (see figure 3(d)), just as we would in regular, incoherent SIM. This improvement occurs because the field extraction and data analysis procedure described above stitches the resulting reciprocal space images together to effectively double the extent of the total CTF (red solid line in figure 3(e)), compared to the physical CTF (dotted red circle in figure 3(e)).

A similar two-fold increase in lateral resolution can be seen when we image the object using widefield SHG (figure 3(f)), and switch to using the SHG-SIM results in a significantly sharper image (figure 3(g)). This improvement is due to an almost four-fold extended total CTF (see figure 3(h)). First, the extent of the physical CTF for widefield

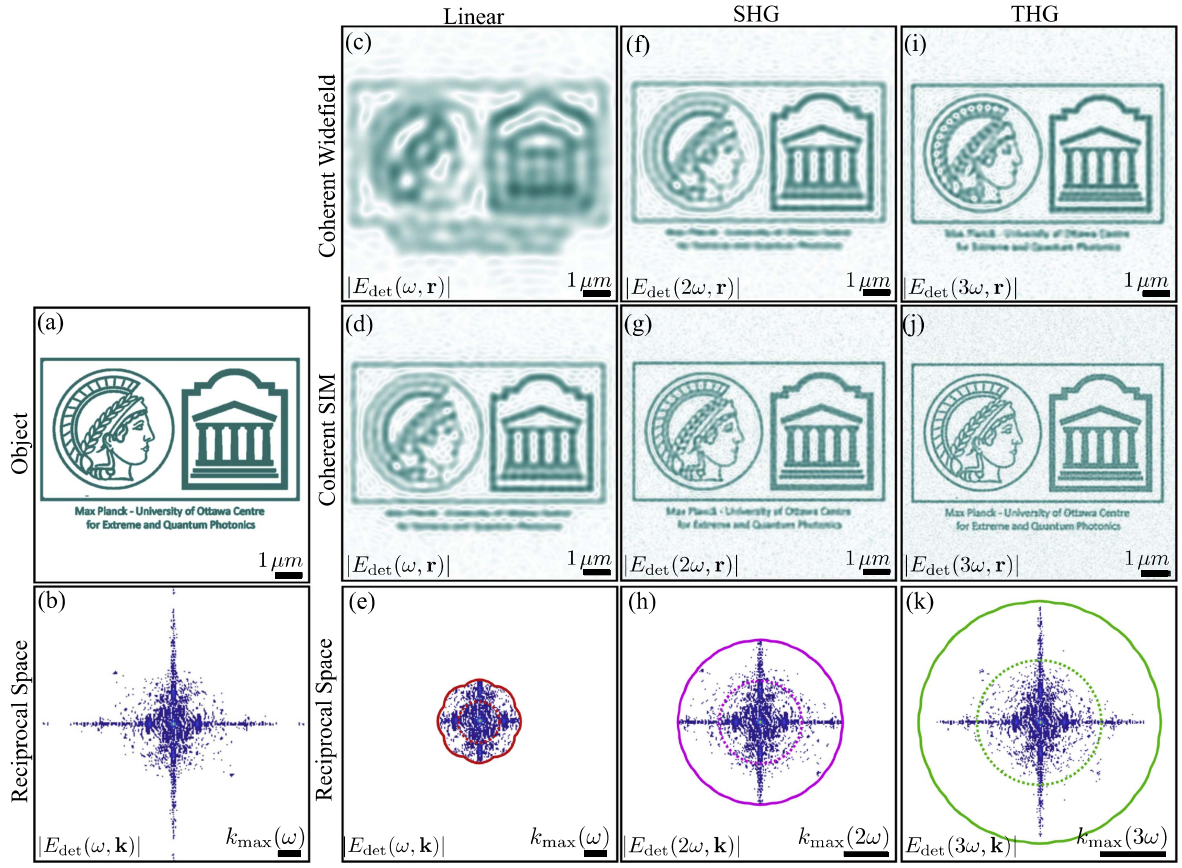

Figure 3. Simulated lateral resolution improvement using coherent SIM schemes. The simulations were performed assuming SNR = 300. (a) Original object with feature sizes below 50 nm and (b) the FT of the object. The object is poorly resolved using only (c) conventional coherent widefield microscopy, but (d) coherent SIM does provide somewhat better resolution because (e) the extent of the total CTF is doubled. The image features become also sharper with (f) widefield SHG or (i) widefield THG, but are significantly better resolved by the (g) SHG-SIM and (j) THG-SIM. The improvement using the SIM schemes occurs because each SIM extends the total CTF by almost a factor of (e) two, (h) four and (k) six, respectively (solid lines). Note that k_{max} is doubled (tripled) for SHG (THG) (see dotted circles).

SHG is doubled by the increase in the highest detectable transverse spatial-frequency component $k_{\mathrm{max}}(2\omega)$ (see magenta dotted circle in figure 3(h)). Second, the proposed SHG-SIM scheme is used to further double the extent of the CTF (see magenta solid line in figure 3(h)). Finally, if the widefield THG response of the object can be collected in a similar manner, an already a relatively well resolved image can be formed (figure 3(i)), and by switching to THG-SIM the resolution is further doubled (see figure 3(j)) in total resulting almost to a six-fold extended CTF when compared to the physical CTF at the fundamental wavelength. This is because $k_{\mathrm{max}}(3\omega)$ is tripled for THG (green dotted circle in figure 3(k)), while the extent of the total CTF is further doubled using the proposed SIM scheme up to a six-fold increase when compared to the extent of the fundamental CTF (see green solid line in figure 3(k)).

Next we quantify the achievable resolution and the resolution improvement by the proposed nonlinear coherent SIM scheme. We note that several approaches to quantify resolution exist and fall into two main categories [44, 45]. In the first, the width of the coherent PSF is used as the metric for lateral resolution [45]. The benefit of this metric is that because the PSF and the CTF are Fourier pairs, this definition is related to the cutoff frequency of the CTF and is thus

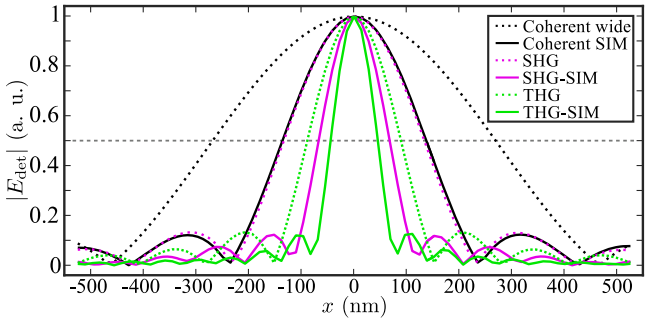

Figure 4. The calculated PSFs for coherent widefield (dotted black), coherent SIM (solid black), widefield SHG (dotted magenta), SHG-SIM (solid magenta), widefield THG (dotted green) and THG-SIM (solid green). The incident wavelength is $\lambda = 1064$ nm and NA = 1.4. The lateral resolutions calculated using the Rayleigh criterion are 464 nm, 235 nm, 152 nm, 118 nm and 77 nm, respectively.

closely related to the Rayleigh limit. In addition, this metric is independent of the possible phase-relation of the scattering objects. In order to quantify our results this way, consider the PSF of the system in each case, as shown in figure 4. We adopt the Rayleigh criterion to define the lateral resolution as the distance from the peak of the PSF to the first minimum.

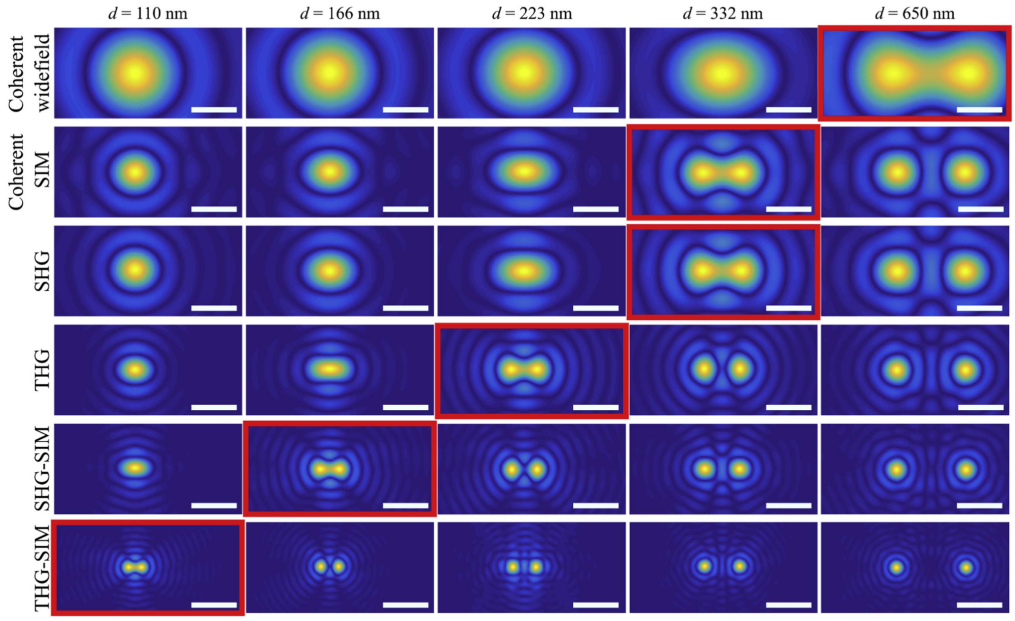

Figure 5. Simulations of two closely spaced objects, separated by distance $d = 110$ nm, 166 nm, 223 nm, 332 nm and 650 nm. Scale bars are 500 nm. Red solid rectangles highlight the shortest distance d when the objects are still resolved for the given imaging modality.

Whereas the coherent widefield PSF has a lateral resolution of 464 nm, linear coherent SIM doubles the upper bound on the captured reciprocal space information, almost halving the resolution to 235 nm. Widefield SHG has an identical lateral resolution of 235 nm, which is again almost doubled by SHG-SIM to 118 nm. Widefield THG provides a lateral resolution of 152 nm, with THG-SIM cutting the resolution down to 77 nm. Note that our nonlinear SIM scheme also surpasses the Abbe limit calculated for the harmonic wavelengths, where a lateral resolution of 190 nm (127 nm) is expected if incident light with wavelength of 532 nm (355 nm) is used.

In the second category, two objects separated by a short distance are imaged, and the resolution is defined as the minimum distance d when the dip in the signal between the objects is at 81% of either maxima, commonly called the Rayleigh criterion [45]. In order use this approach to quantify the achievable resolution, we simulate imaging of two such closely spaced objects by using the mentioned coherent illumination modalities while varying the distance d. From this data, the achievable resolutions for conventional coherent widefield, coherent SIM and widefield SHG, widefield THG, SHG-SIM and THG-SIM modalities are calculated to be 650 nm, 332 nm, 223 nm, 166 nm and 110 nm, respectively (see figure 5). We note that this approach depends on the possible phase-difference between the objects. Our results consider two objects scattering in-phase. If the objects would scatter in phase quadrature, the achievable resolution would coincide with what is achievable using incoherent illumination, while out-of-phase scattering objects could be even better resolved [45].

Next we discuss the potential of the proposed SIM scheme for label-free imaging of biological samples. Since we propose to measure the relatively weak SHG and THG signals using a widefield configuration [29–31], one might assume that the required high peak intensities at the sample would restrict the applicability of the technique to inorganic samples. But as a recent experimental SHG holographic widefield experiment shows, realistic SNRs and imaging speeds can be achieved already with peak intensities on the order of 300 MW cm^{-2} if sensitive electron multiplying charge coupled device (EMCCD) cameras are used [46]. We note that this peak intensity level is approximately three orders of magnitude smaller than what is conventionally used in nonlinear laser-scanning microscopy [15–17], and as such is not expected to harm biological samples. Therefore we believe that even living samples could be imaged. We were not able to find experimental studies using widefield THG microscopy. But since several widefield CARS schemes exist utilizing thus a nonlinear process of same order for contrast [40], we believe that also THG-SIM is feasible.

We also estimate how quickly a SIM image could be formed. Based on our simulations, a SNR of about 300 seems more than adequate to provide high-quality images. According to [46], such a SNR could be achieved with an EMCCD camera using integration times of about 50 ms per widefield SHG image. We record four images for the detected field reconstruction, and estimate that similar to conventional incoherent SIM, seven reconstructed fields extend sufficiently the effective CTF and increase the resolution [10]. Therefore, in total 28 images need to be recorded, resulting in imaging speed of about 1.4 s per SHG-SIM image, which is similar to the imaging speeds of conventional nonlinear laser-scanning microscopes. In addition, we believe that the imaging speed could be further improved by using holographic techniques in the reconstruction of the detected field [46], or by using amplified fs-laser systems for excitation [30, 31].

Next, we consider the robustness of the technique in terms of other sources of noise, artifacts and imaging aberrations. In general due to its nonlinear origin, the detected

image field will be relatively weak, which might complicate the field reconstruction [47]. In addition, the coherent imaging system is susceptible to speckle noise. Therefore, additional measures to improve the SNR, the measurement accuracy and consequent image quality might prove to be beneficial, including off-axis holography or averaging over multiple reconstructed fields [48]. Here, we also assume that the CTF of the imaging system is ideal and entirely known. In practise, the imaging system can have aberrations which will change the CTF accordingly, and the precise CTF may not be entirely known. Therefore, additional calibration of the imaging system may prove useful.

Most importantly we note that the proposed SIM scheme is based on the intrinsic nonlinear optical response of the object, and thus does not require labeling that can compromise studies of sensitive or live objects. For simplicity, we assume in the simulations that the object scatters similarly for linear, SHG and THG light meaning that in practice each modality provides identical imaging contrast. In practice that is not the case. It is well known that SHG from biological tissues is mostly due to collagen fibers [15], and therefore SHG microscopy has been found to be a useful tool to study collagen organization and changes in tissue morphology due to many diseases/disorders [14, 15, 28]. On the other hand, THG microscopy has been found to be a useful tool for visualizing and studying lipid molecules [16–18]. As long as the widefield SHG or THG response from the object is observed [29–31], this technique can be used to significantly improve the lateral resolution. Even though widefield modalities in general have slightly worse lateral resolution compared to laser-scanning microscopy, the achievable resolution is still significantly improved by our technique. The proposed SIM schemes provide clearly improved lateral resolution than laser-scanning SHG (THG) microscopy, beating these techniques roughly by a factor of 3.2 (3.9) [43]. In addition, the proposed scheme could be generalized to other nonlinear processes such as widefield CARS with similar lateral resolution well beyond the diffraction limit.

It is also worth noting that during our mathematical derivation we assumed that the second- and third-order nonlinear susceptibility tensors can be approximated as scalars. Clearly that assumption may not always hold as many biological materials are birefringent, leading to polarization dependent nonlinear response. Interestingly, these effects can provide valuable microscopic information of the studied system, as has been shown in many laser-scanning SHG studies [15, 28, 49, 50]. Therefore, it would be intriguing to investigate further how the proposed widefield nonlinear SIM schemes could be combined with polarization-sensitive techniques.

While our proposed scheme improves the lateral resolution, the axial resolution is not affected. But we note that the traditional SIM can be extended to provide also axial super-resolution [51]. Therefore, we are confident that our proposed nonlinear coherent SIM scheme could be similarly extended to provide both lateral and axial super-resolution. But as the sample thickness increases, propagation effects may complicate the technique and consequent data analysis. For example, speckle noise may play a stronger role and should therefore be accounted for [48]. In addition, phase-matching effects become more important complicating the data analysis [22, 52].

4. Conclusion

In conclusion, we propose a widefield coherent nonlinear SIM scheme based on spatially modulating the phase of the incident field and consequent interferometric detection of the emitted complex-valued field. We have numerically shown that the lateral resolution can be drastically improved by taking advantage of the nonlinear optical response of the object. In particular we have shown that if the second-harmonic (third-harmonic) emission from the object can be collected, the achievable resolution can be increased four-fold (six-fold). Since the nonlinear response of the object is intrinsic, the proposed technique can be used for label-free imaging. Our proposed method promises to open up new avenues for biological imaging and for biomedical diagnostics.

Funding

The Canada Excellence Research Chairs; Natural Sciences and Engineering Research Council of Canada (RGPin-418389-2012); Finnish Cultural Foundation (00150020).

References

[1] Abbe E 1873 Beiträge zur theorie des mikroskops und der mikroskopischen wahrnehmung *Arkiv. Mikroskop. Anat.* **9** 413–8
[2] Huang B, Bates M and Zhuang X 2009 Super resolution fluorescence microscopy *Annu. Rev. Biochem.* **78** 993–1016
[3] Hell S W and Wichmann J 1994 Breaking the diffraction resolution limit by stimulated emission: stimulated-emission-depletion fluorescence microscopy *Opt. Lett.* **19** 780–2
[4] Willig K I, Rizzoli S O, Westphal V, Jahn R and Hell S W 2006 STED microscopy reveals that synaptotagmin remains clustered after synaptic vesicle exocytosis *Nature* **440** 935–9
[5] Betzig E, Patterson G H, Sougrat R, Lindwasser O W, Olenych S, Bonifacino J S, Davidson M W, Lippincott-Schwartz J and Hess H F 2006 Imaging intracellular fluorescent proteins at nanometer resolution *Science* **313** 1642–5
[6] Rust M J, Bates M and Zhuang X 2006 Sub-diffraction-limit imaging by stochastic optical reconstruction microscopy (STORM) *Nat. Methods* **3** 793–6
[7] Müller C B and Enderlein J 2010 Image scanning microscopy *Phys. Rev. Lett.* **104** 198101
[8] Sheppard C J R, Shalin B N and Heintzmann R 2013 Superresolution by image scanning microscopy using pixel reassignment *Opt. Lett.* **38** 2889–92
[9] Heintzmann R and Cremer C G 1999 Laterally modulated excitation microscopy: improvement of resolution by using a diffraction grating *Proc. SPIE* **3568** 185–96

[10] Gustafsson M G L 2000 Surpassing the lateral resolution limit by a factor of two using structured illumination microscopy *J. Microsc.* **198** 82–7
[11] Heintzmann R, Jovin T M and Cremer C 2002 Saturated patterned excitation microscopy—a concept for optical resolution improvement *J. Opt. Soc. Am.* A **19** 1599–609
[12] Gustafsson M G L 2005 Nonlinear structured-illumination microscopy: wide-field fluorescence imaging with theoretically unlimited resolution *Proc. Natl Acad. Sci. USA* **102** 13081–6
[13] Rego E H, Shao L, Macklin J J, Winoto L, Johansson G A, Kamps-Hughes N, Davidson M W and Gustafsson M G 2012 Nonlinear structured-illumination microscopy with a photoswitchable protein reveals cellular structures at 50-nm resolution *Proc. Natl Acad. Sci. USA* **109** E135–43
[14] Strupler M, Pena A M, Hernest M, Tharaux P L, Martin J L, Beaurepaire E and Schanne-Klein M C 2007 Second harmonic imaging and scoring of collagen in fibrotic tissues *Opt. Express* **15** 4054–65
[15] Chen X, Nadiarynkh O, Plotnikov S and Campagnola P J 2012 Second harmonic generation microscopy for quantitative analysis of collagen fibrillar structure *Nat. Protocols* **7** 654–69
[16] Débarre D, Supatto W, Pena A M, Fabre A, Tordjmann T, Combettes L, Schanne-Klein M C and Beaurepaire E 2006 Imaging lipid bodies in cells and tissues using third-harmonic generation microscopy *Nat. Methods* **3** 47–53
[17] Olivier N *et al* 2010 Cell lineage reconstruction of early zebrafish embryos using label-free nonlinear microscopy *Science* **329** 967–71
[18] Bautista G, Pfisterer S G, Huttunen M J, Ranjan S, Kanerva K, Ikonen E and Kauranen M 2014 Polarized THG microscopy identifies compositionally different lipid droplets in mammalian cells *Biophys. J.* **107** 2230–6
[19] Littleton B, Lai K, Longstaff D, Sarafis V, Munroe P, Heckenberg N and Rubinsztein-Dunlop H 2007 Coherent super-resolution microscopy via laterally structured illumination *Micron* **38** 150–7
[20] Mudassar A A and Hussain A 2010 Super-resolution of active spatial frequency heterodyning using holographic approach *Appl. Opt.* **49** 3434–41
[21] Chowdhury S, Dhalla A-H and Izatt J 2012 Structured oblique illumination microscopy for enhanced resolution imaging of non-fluorescent, coherently scattering samples *Biomed. Opt. Express* **3** 1841–54
[22] Boyd R W 2003 *Nonlinear Optics* (New York: Academic)
[23] Denk W, Strickler J H and Webb W W 1990 Two-photon laser scanning fluorescence microscopy *Science* **248** 73–6
[24] Gannaway J N and Sheppard C J R 1978 Second-harmonic imaging in the scanning optical microscope *Opt. Quantum Electron.* **10** 435–9
[25] Yelin D and Silberberg Y 1999 Laser scanning third-harmonic-generation microscopy in biology *Opt. Express* **5** 169–75
[26] Squier J, Muller M, Brakenhoff G and Wilson K R 1998 Third harmonic generation microscopy *Opt. Express* **3** 315–24
[27] Freudiger C W, Min W, Saar B G, Lu S, Holtom G R, He C, Tsai J C, Kang J X and Xie X S 2008 Label-free biomedical imaging with high sensitivity by stimulated Raman scattering microscopy *Science* **322** 1857–61
[28] Lee H, Huttunen M J, Hsu K-J, Partanen M, Zhuo G-Y, Kauranen M and Chu S-W 2013 Chiral imaging of collagen by second-harmonic generation circular dichroism *Biomed. Opt. Express* **4** 909–16
[29] Peterson M D, Hayes P L, Martinez I S, Cass L C, Achtyl J L, Weiss E A and Geiger F M 2011 Second harmonic generation imaging with a kHz amplifier [Invited] *Opt. Mater. Express* **1** 57–66
[30] Cheng L C, Chang C Y, Lin C Y, Cho K C, Yen W C, Chang N S, Xu C, Chen Y D and Chen S J 2012 Spatiotemporal focusing-based widefield multiphoton microscopy for fast optical sectioning *Opt. Express* **20** 8939–48
[31] Macias-Romero C, Didier M E, Jourdain P, Marquet P, Magistretti P, Tarun O B, Zubkovs V, Radenovic A and Roke S 2014 High throughput second harmonic imaging for label-free biological applications *Opt. Express* **22** 31102–12
[32] Beeker W P, Groß P, Lee C J, Cleff C, Offerhaus H L, Fallnich C, Herek J L and Boller K-J 2009 A route to sub-diffraction-limited CARS Microscopy *Opt. Express* **17** 22632–8
[33] Hajek K M, Littleton B, Turk D, McIntyre T J and Rubinsztein-Dunlop H 2010 A method for achieving super-resolved widefield CARS microscopy *Opt. Express* **18** 19263–72
[34] Kim H, Bryant G W and Stranick S J 2012 Superresolution four-wave mixing microscopy *Opt. Express* **20** 6042–51
[35] Park J H, Lee S-W, Lee E S and Lee J Y 2014 A method for super-resolved CARS microscopy with structured illumination in two dimensions *Opt. Express* **22** 9854–70
[36] Field J J, Wernsing K A, Domingue S R, Motz A M A, DeLuca K F, Levi D H, DeLuca J G, Young M D, Squier J A and Bartels R A 2016 Superresolved multiphoton microscopy with spatial frequency-modulated imaging *Proc. Natl Acad. Sci. USA* **113** 6605–10
[37] Masihzadeh O, Schlup P and Bartels R A 2009 Enhanced spatial resolution in third-harmonic microscopy through polarization switching *Opt. Lett.* **34** 1240–2
[38] Hoover E E *et al* 2012 Eliminating the scattering ambiguity in multifocal, multimodal, multiphoton imaging systems *J. Biophotonics* **5** 425–36
[39] Evans C L, Potma E O, Puoris'haag M, Côté D, Lin C P and Xie X S 2005 Chemical imaging of tissue *in vivo* with video-rate coherent anti-Stokes Raman scattering microscopy *Proc. Natl Acad. Sci. USA* **102** 16807–12
[40] Heinrich C, Hofer A, Ritsch A, Ciardi C, Bernet S and Ritsch-Marte M 2008 Selective imaging of saturated and unsaturated lipids by wide-field CARS-microscopy *Opt. Express* **16** 2699–708
[41] Schnars U and Jüptner W 1994 Direct recording of holograms by a CCD target and numerical reconstruction *Appl. Opt.* **33** 179–81
[42] Foi A, Trimeche M, Katkovnik V and Egiazarian K 2008 Practical Poissonian-Gaussian noise modeling and fitting for single-image raw-data *IEEE Trans. Image Process.* **17** 1737–54
[43] Chen S Y, Hsieh C S, Chu S W, Lin C Y, Ko C Y, Chen Y C, Tsai H J, Hu C H and Sun C K 2006 Noninvasive harmonics optical microscopy for long-term observation of embryonic nervous system development *in vivo J. Biomed. Opt.* **11** 054022
[44] Wicker K and Heintzmann R 2014 Resolving a misconception about structured illumination *Nat. Photon.* **8** 342–4
[45] Van Aert S, Van Dyck D and Arnold J 2006 Resolution of coherent and incoherent imaging systems reconsidered-Classical criteria and a statistical alternative *Opt. Express* **14** 3830–9
[46] Masihzadeh O, Schlup P and Bartels R A 2010 Label-free second harmonic generation holographic microscopy of biological specimens *Opt. Express* **18** 9840–51
[47] Smith D R, Winters D G, Schlup P and Bartels R A 2012 Hilbert reconstruction of phase-shifted second-harmonic holographic images *Opt. Lett.* **37** 2052–4

[48] Cuche E, Marquet P and Depeursinge C 1999 Simultaneous amplitude-contrast and quantitative phase-contrast microscopy by numerical reconstruction of Fresnel off-axis holograms *Appl. Opt.* **38** 6994–7001

[49] Le Floc'h V, Brasselet S, Roch J F and Zyss J 2003 Monitoring of orientation in molecular ensembles by polarization sensitive nonlinear microscopy *J. Phys. Chem.* B **107** 12403–10

[50] Winters D G, Smith D R, Schlup P and Bartels R A 2012 Measurement of orientation and susceptibility ratios using a polarization-resolved second-harmonic generation holographic microscope *Biomed. Opt. Express* **3** 2004–11

[51] Gustafsson M G, Shao L, Carlton P M, Wang C R, Golubovskaya I N, Cande W Z, Agard D A and Sedat J W 2008 Three-dimensional resolution doubling in wide-field fluorescence microscopy by structured illumination *Biophys. J.* **94** 4957–70

[52] Yelin D and Silberberg Y 1999 Laser scanning third-harmonic-generation microscopy in biology *Opt. Express* **5** 169–75